ELSEVIER

Chemical Engineering Journal 139 (2008) 363–379

Chemical Engineering Journal

www.elsevier.com/locate/cej

Numerical simulation of the gas–liquid flow in a laboratory scale bubble column Influence of bubble size distribution and non-drag forces

M. Elena Díaz [a], Alfredo Iranzo [b], Daniel Cuadra [b], Rubén Barbero [b], Francisco J. Montes [a,*], Miguel A. Galán [a]

[a] *Departamento de Ingeniería Química y Textil, University of Salamanca, Plaza de los Caídos 1-5, 37008 Salamanca, Spain*
[b] *Análisis-DSC, Nuestra Señora de la Luz, 21 Local Izqdo, 28025 Madrid, Spain*

Received 29 May 2007; received in revised form 10 August 2007; accepted 13 August 2007

Abstract

In the present work, a computational model based on an Eulerian–Eulerian approach was used for the simulation of the transient two-phase flow in a rectangular partially aerated bubble column. Superficial gas velocities (U_G) ranging from 0.24 to 2.30 cm/s were used throughout both the experiments and the simulations. The calculated results were verified by comparing them with experimental data including measurements of gas hold-up, plume oscillation period (POP) and Sauter mean bubble diameter. The study shows the effect of mesh refinement, time-step and physical model selection, the latter regarding the role of bubble size distribution and non-drag forces, on the computational results. According to the results presented here, the representation of bubble populations using multiple size groups (MUSIG model) instead of a single group improves the prediction of the experimental parameters under study. Additionally, the results obtained after including the virtual mass force term do not differ considerably from those obtained including only the drag force. On the contrary, as a consequence of introducing the lift force term into the model, the gas hold-up is overestimated and a non-symmetric bubble plume oscillation appears, a fact that is not experimentally observed.

Keywords: Bubble column; Simulation; CFD; Gas–liquid flow; Coalescence; Break-up

1. Introduction

Bubble columns are multiphase reactors where the gas, that constitutes the dispersed phase, is distributed at the bottom of the column and rises as bubbles through the liquid, which constitutes the continuous (stationary or flowing) phase. These equipments are used in many important industrial processes involving gas–liquid systems in the chemical (e.g. manufacture of synthetic fuels), biological (e.g. fermentors) and petrochemical (e.g. coal liquefaction) areas. This is mainly due to the advantages that they present over other multiphase reactors, advantages that include low price, simple construction, low operational costs, efficient mixing and high mass and heat transfer efficiency (large interfacial areas). Despite the extended industrial applications of bubble columns, there are still some unanswered questions regarding their design and scale-up, basically due to the partial knowledge of the fluid dynamics of the gas–liquid flow. In this context, the use of computational fluid dynamics (CFD) becomes an essential tool since it can predict and describe the fluid hydrodynamics on both local and global scale. In this way, numerous multiphase flow CFD studies have been published in the last 10 years. However, several modeling problems are yet to be solved due to the complex hydrodynamic characteristics, the inherent unsteadiness of the liquid flow generated by the passage of bubbles or the uncertainty on the interfacial interactions.

Two main approaches are often used when modeling gas–liquid flow in bubble columns: Euler–Euler (E–E) [1–7] and Euler–Lagrange (E–L) [8–11]. The E–E approach (the two-fluid model) considers the gas and liquid phases in an Eulerian

Abbreviations: CFL, Courant, Freidricks, Levy; E–E, Euler–Euler model; E–L, Euler–Lagrange model; DBVF, dispersed bubble vortical flow; FDVF, fully developed vortical flow; POP, plume oscillation period; TVF, transitional vortical flow

* Corresponding author. Tel.: +34 923 294479; fax: +34 923 294574.
E-mail address: javimon@usal.es (F.J. Montes).

1385-8947/$ – see front matter © 2007 Elsevier B.V. All rights reserved.
doi:10.1016/j.cej.2007.08.015

Nomenclature

B, C	mass source due to breakage and coalescence, respectively (kg/m^3 s)
C_D	drag coefficient
C_L	lift coefficient
C_{VM}	virtual mass coefficient
$C_{\varepsilon 1}$	parameter in k–ε model
$C_{\varepsilon 2}$	parameter in k–ε model
C_μ	parameter in k–ε model
d_b	bubble diameter (m)
d_{32}	global mean Sauter diameter (m)
Eo_1	Eötvös number
f_{BV}	break-up fraction
f_i	volume fraction of bubbles of class i
F_B	calibration coefficient
F_{CT}	calibration coefficient
F_i	global mean size fraction of bubble group i
$\underline{F}$	interphase momentum forces between phases vector (N)
g	specific break-up rate of bubbles (1/s)
$\underline{g}$	gravity vector (m/s^2)
G	specific coalescence rate of bubbles (m^3/s)
h_f	critical film thickness (m)
h_0	initial film thickness (m)
k	turbulent kinetic energy per unit mass (m^2/s^2)
m	mass (kg)
M	Morton number
N	number of groups in multisize bubbles model
p	pressure (N/m^2)
r_{ij}	equivalent radius (m)
S_i	mass source term in gas phase equation (mass conservation) (kg/m^3 s)
S_{ij}	cross-sectional area of colliding particles (m^2)
t	time (s)
t_{ij}	time required for coalescence (s)
u_{ti}	turbulent velocity (m/s)
U_G	gas superficial velocity (m/s)
v	vertical component of the velocity vector (m/s)
$\underline{v}$	velocity vector (m/s)
V_b	terminal velocity (m/s)
x, y, z	spatial coordinates (width, length and depth, respectively) (m)

Greek letters

α	volume fraction
γ	surface tension coefficient (N/m)
ε	eddy dissipation rate (m^2/s^3)
μ	viscosity (kg/m s)
ν	kinematic viscosity (m^2/s)
ξ	size of eddies in the inertial sub-range of isotropic turbulence
ρ	density (kg/m^3)
σ_k	constant in k–ε model
σ_ε	constant in k–ε model
σ	turbulent Prandtl number
τ_{ij}	contact time (s)
$\underline{\underline{\tau}}$	shear stress tensor (kg/m s^2)
χ_c	critical energy for break-up
ω_c	curl of continuous phase velocity (1/s)

Superscripts

+, −	gain or loss
D	drag
LF	lift force
VM	virtual mass

Subscripts

eff	effective
g	gas
i	class of bubbles
k, m	l (liquid phase)/g (gas phase)
l	liquid
lam	laminar
t	turbulent

representation as two interpenetrating fluids. The phases interact through the interphase transfer terms and individual solutions of the mass and momentum balances are needed [12]. On the other hand, the E–L approach tracks each bubble separately while the liquid phase is treated as a continuum. In this way, separate force balance equations are solved for each individual bubble while both phases interact through a source term in the momentum equation. The use of the E–L model allows the introduction of coalescence, break-up and collisions relative easily, but the number of bubbles is limited and it can be computationally expensive. Additionally, E–E simulations are applicable to a wider range of volume fractions, while E–L is restricted to low particle volume fractions as the fraction of volume taken by the particles is not included in the continuous phase calculation. Furthermore, the use of high order discretization schemes with the E–E approach solves the problem of the higher numerical diffusion obtained in comparison with the E–L approach [13], a fact described by Sokolichin et al. [14].

Several attempts have been made in order to model the hydrodynamics of bubble plumes in bubble columns [1,5,8,12,15,16]. Bubble plumes were first described by Chen et al. [17] and Tzeng at al. [18] in two-dimensional (2D) uniform aerated bubble columns and by Chen et al. [19] in a cylindrical (three-dimensional (3D)) uniform aerated bubble column. These authors observed, at increasing values of gas superficial velocities (U_G), two flow regimes: the dispersed bubble and the coalesced bubble flow regimes. At the same time, the coalesced bubble flow regime was subdivided into the vortical–spiral (3D bubble column) or vortical (2D bubble column) regime and the turbulent flow regime. The vortical flow regime presented four different flow regions: descending, vortical, fast bubble and central plume. Nevertheless, the four-region flow described by Tzeng et al. [18] evolved, at increasing values of U_G, to a three-region flow consisting on one central fast bubble region together with the vortical and descending flow regions. Furthermore, the

four-region flow was not observed for bubble columns of width less than approximately 20 cm. The fast bubble flow region is very characteristic of this type of flow since it was shown to describe a wavelike motion in 2D bubble columns and a spiral motion in 3D bubble columns [19]. In line with the existence of the vortical flow regime and the experiments performed by Tzeng et al. [18] with non-uniform gas injection, Becker et al. [15] studied the resulting flow patterns when using an unsymmetrical gas distribution. The bubble plume formed showed an oscillatory movement with a behavior equivalent to that of the fast bubble region described by Tzeng et al. [18]. After the experiments reported by Becker et al. [15] many authors have studied partially aerated bubble columns [1–3,12,16,20–25]. Among them, Diaz et al. [25] showed that in a partially aerated bubble column the dispersed bubble and turbulent flow regimes are not observed prevailing the vortical flow regime at all values of U_G. Also, Diaz et al. [25] described the existence of three flow patterns included in the generic vortical flow regime: the dispersed bubble vortical flow (DBVF), the transition vortical flow (TVF) and the fully developed vortical flow (FDVF). The differences between these three flow regimes were based on the bubble size distribution, frequency of oscillation of the bubble plume as well as on the apparent aeration of the bubble column along its height.

Detailed computational studies have been performed to simulate the dynamics of bubble plumes in bubble columns. Good agreement between experimental and computational data on the oscillating behavior of the bubble plume was obtained by Becker at al. [15]. Pfleger et al. [5] concluded that 3D simulations and the consideration of the well known k–ε turbulence model for the continuous phase are needed in order to reproduce the periodic movement of the bubble plume. According to Pfleger's studies, 2D simulations do not show this oscillating behavior due to an over prediction of the turbulent energy in the fluid. Mudde and Simonin [12] confirmed Pfleger's findings [5] regarding the need of a 3D simulation for the correct prediction of the oscillating flow. Furthermore, Mudde and Simonin [12] reported that, in order to accurately calculate the plume oscillation period (POP) and the amplitude of the velocity field, the virtual mass force together with the drag force should be considered. Sokolichin and Eigenberger [1] also showed that a 3D simulation with the consideration of the k–ε model leads to a satisfactory agreement with experimental data. However, Pan et al. [7] reported that 2D simulation of the dispersed bubbly flow in a 2D bubble column captures the key features of large structures and reproduces mean flow quantities. Buwa et al. [16] reported good agreement between experimental and simulated POPs. According to their results [16], the representation of the gas sparger does not have significant influence on the simulated POP results being the bubble size distribution the determining variable. Oey et al. [26] found that the numerical diffusion caused by the particular discretization schemes used for the convective terms affected the simulation results in such a way that if considerable numerical error occurs, the calculated results do not show a transient behavior. Bech [4] studied the effect of different dynamic turbulence models. According to Bech's results, the simple mixing length turbulence model leads to the best results for the prediction of the POP while, qualitatively, the k–ω model leads to a more accurate reproduction of the bubble plume than the classic k–ε model.

Most of the simulations performed to model the hydrodynamics of bubble plumes mentioned above have used the assumption of a single bubble size distribution. This assumption may be valid under the dispersed bubble flow regime since the interaction between bubbles is low and the bubble size distribution is very narrow. However, as U_G increases, coalescence and break-up phenomena become important giving as a result a wide bubble size distribution, a fact that differs considerably from a single mean bubble size consideration. Several models have been used to calculate coalescence and break-up frequencies [27–29] while, more recently, these models have been implemented into CFD codes [16,30–33]. The implementation was based on the solution of the mass and momentum equations for all bubble sizes [31], on the solution of only the mass transfer equation for all bubble sizes while they share a common velocity field [30] or on the consideration of equilibrium between coalescence and break-up frequencies [32]. Buwa et al. [16] implemented different coalescence and break-up models and compared their results with experimental data, finding a qualitatively better agreement with the breakage probability proposed by Lehr and Mewes [32]. Despite the implementation of multiple size models into the CFD codes and the importance of simulating the evolution of the bubble size distribution, only a few studies have included them into the simulations [34,35].

In this paper, a full 3D E–E modeling of the hydrodynamics of unsteady flow structures developed in a symmetrically aerated 2D bubble column is presented at different values of U_G, allowing the study of the DBVF, TVF and FDVF regimes. The commercial code CFX 10.0 from Ansys, Inc., based on the finite volume technique, is used. The gas is considered as the dispersed phase in the form of spherical bubbles while the liquid is considered as the continuous phase. Single and multiple size group models are used and the results are compared. Furthermore, the effect of the inclusion of non-drag forces (virtual mass and lift forces) on the hydrodynamic characteristics of the flow is studied. Qualitative validation of the proposed model is achieved by comparison of experimental images of the flow inside the lab bubble column with snapshots of the calculated flow characteristics. Quantitative validation is based on experimental measurements of the gas hold-up and the POP at different U_G values. Also the evolution of the predicted global Sauter diameter is compared to the experimental values obtained by means of a photographic technique. Conclusions about the use of multiple bubble size versus single bubble size models as well as the inclusion of non-drag forces are presented in the following sections of this paper.

2. Hydrodynamic equations and computational model

Evaporation and condensation processes are considered negligible and inter-phase mass transfer is not included in this analysis. The fluids are assumed incompressible and isothermal.

2.1. Mass conservation equation

Considering the simplifications previously mentioned, the Reynolds averaged form of the mass conservation equation in the Eulerian framework is given by Eqs. (1) and (2):

$$\text{liquid phase}: \quad \frac{\partial}{\partial t}(\rho_l \alpha_l) + \nabla \cdot (\rho_l \alpha_l \underline{v}_l) = 0 \tag{1}$$

$$\text{gas phase}: \quad \frac{\partial}{\partial t}(\rho_g \alpha_g f_i) + \nabla \cdot (\rho_g \alpha_g \underline{v}_g f_i) = S_i \tag{2}$$

where α_k is the phase volume fraction, ρ_k the phase density, $\underline{v}_k$ the phase velocity vector (being k = l the liquid phase and k = g the gas phase), f_i the volume fraction of bubbles of class i ($f_i = \alpha_{g_i}/\alpha_g$) and S_i is the mass source term that takes into account the death and birth of bubbles caused by break-up and coalescence processes. With the above consideration of zero inter-phase mass transfer, it is clear that $S_i = 0$ under the assumption of constant and uniform bubble size, assumption only valid at low U_G values. However, N groups of bubbles need to be considered at sufficiently large U_G values at which bubbles of different diameters exist (see Section 5.2). In this case, S_i is calculated as

$$S_i = \{B_i^+ - B_i^- + C_i^+ - C_i^-\} \tag{3}$$

where i varies from 1 to N ($i = 1, 2, \ldots, N$), B and C stand for breakup and coalescence and + and − for gain or loss, respectively. The multiple size group model considered in this work uses equal diameter discretization. Ten groups of bubbles ranging from diameters of 1 to 10 mm, respectively, are considered (see Table 1).

The simulations of the break-up phenomena are performed using the Luo and Svendsen model [28], based on the theory of isotropic turbulence and probability. This model assumes binary break-up and contains no adjustable parameters. The break-up rate of bubbles of volume v_j into bubbles of volume v_i is given by

$$g(v_j; v_i) = 0.923 F_B (1 - \alpha_g) \left(\frac{\varepsilon}{d_j^2}\right)^{1/3} \int_{\xi_{min}}^{1} \frac{(1+\xi)^2}{\xi^{11/3}} \, e^{-\chi_c} \, d\xi \tag{4}$$

where ε is the turbulent energy dissipation rate, F_B the calibration coefficient, d the bubble diameter, ξ the dimensionless size of eddies in the inertial sub-range of isotropic turbulence and χ_c is the critical dimensionless energy for break-up given by

$$\chi_c = \frac{12[f_{BV}^{2/3} + (1 - f_{Bv})^{2/3} - 1]\gamma}{2\rho_l \varepsilon^{2/3} d_i^{5/3} \xi^{11/3}} \tag{5}$$

where f_{Bv} is the break-up fraction ($f_{Bv} = m_j/m_i$, being m_i the mass of group i) and γ is the surface tension coefficient. The lower limit of the integration in Eq. (4) is given by

$$\xi_{min} = 11.4 \frac{(1/\varepsilon \, \nu_l^3)^{1/4}}{d_i} \tag{6}$$

where v_l is the liquid kinematic viscosity. Considering the definition of the break-up rate given by Eq. (4), the gain and loss of bubbles of group i due to break-up are given by

$$B_i^+ = \rho_g \alpha_g \left(\sum_{j>i} g(v_j; v_i) f_i \right),$$

$$B_i^- = \rho_g \alpha_g \left(f_i \sum_{j<i} g(v_j; v_i) \right) \tag{7}$$

The Prince and Blanch model [27] is used for the modeling of the coalescence processes. According to this model, coalescence of bubbles takes place after a collision of two bubbles, drainage of the layer of liquid trapped between them and rupture of the resulting liquid film. The first step, the collision, is a result of turbulence, buoyancy or laminar shear. Simulations in this work are performed under the consideration of turbulence as the only contribution to the resulting collision frequency, being buoyancy and laminar shear contributions considered negligible [35]. With this assumption, the rate at which bubbles of size v_i coalesce with bubbles of size v_j to form bubbles of size $v_i + v_j$ is given by

$$Q(v_i; v_j) = F_{CT} S_{ij} (u_{ti}^2 + u_{tj}^2)^{1/2} \, e^{-t_{ij}/\tau_{ij}} \tag{8}$$

where F_{CT} is a calibration factor and S_{ij} is the cross-sectional area of the colliding particles expressed as

$$S_{ij} = \frac{\pi}{4}(d_i + d_j)^2 \tag{9}$$

u_{ti} is the turbulent velocity calculated as

$$u_{ti} = \sqrt{2} \varepsilon^{1/3} d_i^{1/3} \tag{10}$$

and t_{ij} and τ_{ij} are the time required for coalescence and the contact time, respectively:

$$t_{ij} = \left(\frac{\rho_l r_{ij}^3}{16\gamma}\right)^{1/2} \ln\left(\frac{h_0}{h_f}\right), \qquad \tau_{ij} = \frac{r_{ij}^{2/3}}{\varepsilon^{1/3}} \tag{11}$$

where h_0 is the initial film thickness, h_f the critical film thickness when rupture occurs and r_{ij} is the equivalent radius that can be calculated as

$$r_{ij} = \left[\frac{1}{2}\left(\frac{1}{r_i} + \frac{1}{r_j}\right)\right]^{-1} \tag{12}$$

Table 1
Size group discretization

Group number (g)	Diameter of the group (mm)
1	1.45
2	2.35
3	3.25
4	4.15
5	5.05
6	5.95
7	6.85
8	7.75
9	8.65
10	9.55

The calculation of the gain and loss of bubbles of group i due to coalescence can be performed as

$$C_i^+ = (\rho_g \alpha_g)^2 \left(\frac{1}{2} \sum_{j \le i} \sum_{k \le i} Q(v_j; v_k) X_{jki} f_j f_k \frac{m_j + m_k}{m_j m_k} \right),$$

$$C_i^- = (\rho_g \alpha_g)^2 \left(\sum_j Q(v_j; v_k) f_i f_j \frac{1}{m_j} \right) \quad (13)$$

where X_{jki} represents the fraction of mass due to coalescence between groups j and k which goes into group i.

2.2. Momentum conservation equation

Assuming that all bubble groups share a common velocity field [30], the Reynolds averaged form of the momentum conservation equation for each phase is given by Eq. (14):

$$\frac{\partial}{\partial t}(\rho_k \alpha_k \underline{v}_k) + \underline{\nabla} \cdot (\rho_k \alpha_k \underline{v}_k \underline{v}_k) = -\alpha_k \underline{\nabla} p + \rho_k \alpha_k \underline{g} - \underline{\nabla}(\alpha_k \underline{\underline{\tau}}_k) + \underline{F}_{km} \quad (14)$$

where $\underline{g}$ is the gravity vector, p the pressure, assumed to be equal for both phases since the interfacial pressure drop is considered negligible, $\underline{\underline{\tau}}_k$ the phase shear stress tensor and $\underline{F}_{km}$ represents all the inter-phase momentum forces between phase k and m. The consideration of a common velocity field for all bubbles is a simplification that allows for the consideration of higher number of bubble size groups while keeping the computational time under practical limits. Considering a Newtonian fluid, the shear stress tensor is given by

$$\underline{\underline{\tau}}_k = -\mu_{\text{eff},k}(\underline{\nabla} \underline{v}_k + (\underline{\nabla} \underline{v}_k)^{\text{T}}) \quad (15)$$

where $\mu_{\text{eff},k}$ is the effective viscosity of phase k.

2.3. Turbulence modeling

Closure of Eqs. (14) and (15), requires an expression for the eddy viscosities of the gas and the liquid phases. The effective viscosity of the liquid phase, $\mu_{\text{eff},j}$, is calculated as the result of two contributions:

$$\mu_{\text{eff},l} = \mu_{\text{lam}} + \mu_{\text{t},j} \quad (16)$$

where μ_{lam} is the laminar liquid viscosity and $\mu_{\text{t},j}$ is the turbulent liquid viscosity. The last term is calculated using the standard two-equation k–ε turbulence model [36], where k represents the turbulent kinetic energy and ε its dissipation rate. The turbulent viscosity based on the k–ε model is formulated as

$$\mu_{\text{t,l}} = \rho_L C_\mu \frac{k^2}{\varepsilon} \quad (17)$$

being k and ε calculated from their conservation equations [37]. The k–ε model is applied, in this work, with its standard constant values: $C_\mu = 0.09$, $C_{\varepsilon 1} = 1.44$, $C_{\varepsilon 2} = 1.92$, $\sigma_k = 1.0$ and $\sigma_\varepsilon = 1.3$. These constants, although not universal, are commonly used in the case of single-phase flow. No modifications due to the influence of the dispersed phase on the turbulence of the liquid phase are introduced in this work due to the satisfactory results obtained with the standard k–ε model [38] together with the negative effects of introducing bubble induced turbulence terms [39].

The calculation of the turbulent gas viscosity, $\mu_{\text{t,g}}$, is based on the dispersed phase zero equation model [40]:

$$\mu_{\text{t,g}} = \frac{\rho_g}{\rho_l} \frac{\mu_{\text{t,l}}}{\sigma} \quad (18)$$

The parameter σ is a turbulent Prandtl number relating the dispersed phase kinematic eddy viscosity to the continuous phase kinematic eddy viscosity.

2.4. Interphase momentum transfer models

The interphase momentum transfer term in Eq. (14), $\underline{F}_{\text{lg}}$, can be calculated as

$$-\underline{F}_{\text{gl}} = \underline{F}_{\text{lg}} = \underline{F}_{\text{lg}}^D + \underline{F}_{\text{lg}}^{\text{LF}} + \underline{F}_{\text{lg}}^{\text{VM}} \quad (19)$$

$\underline{F}_{\text{lg}}^{\text{D}}$, $\underline{F}_{\text{lg}}^{\text{LF}}$ and $\underline{F}_{\text{lg}}^{\text{VM}}$ are the drag, lift and virtual mass forces. The interphase momentum exchange due to the drag force is given by

$$\underline{F}_{\text{lg}}^{\text{D}} = \frac{3}{4} C_{\text{D}} \alpha_g \rho_l |\underline{v}_g - \underline{v}_l| (\underline{v}_g - \underline{v}_l) \quad (20)$$

where C_{D} represents the drag coefficient that is calculated according to Eq. (12) [41]:

$$C_{\text{D}} = \frac{4}{3} \left(\frac{\rho_l - \rho_g}{\rho_l} \right) \frac{g d_b}{V_b^2} \quad (21)$$

V_b represents the terminal velocity and d_b the bubble diameter. The terminal velocity is calculated as

$$V_b = \frac{\mu_l}{\rho_l d_b} M^{-0.149} \quad (J - 0.857) \quad (22)$$

where M is the Morton number and J is defined as

$$J = \begin{cases} 0.94 H^{0.751} & 2 < H \le 59.3 \\ 3.42 H^{0.441} & H > 59.3 \end{cases} \quad (23)$$

where

$$H = \frac{4}{3} Eo M^{-0.149} \left(\frac{\mu_l}{\mu_{\text{ref}}} \right)^{-0.14} \quad (24)$$

being Eo the Eötvös number and $\mu_{\text{ref}} = 0.0009\ \text{kg m}^{-1}\ \text{s}^{-1}$.

Lift and virtual mass forces have also been included in the study in order to assess its influence on the hydrodynamics of the bubble column. The lift force acts perpendicular to the direction of relative motion of the two phases. The model considered in this work accounts for the shear-induced lift force acting on a dispersed phase in the presence of a rotational continuous phase:

$$\underline{F}_{\text{lg}}^{\text{LF}} = -\underline{F}_{\text{gl}}^{\text{LF}} = \alpha_g \rho_l C_L (\underline{v}_g - \underline{v}_l) \times \omega_c, \qquad \omega_c = \text{curl}(\underline{v}_l) \quad (25)$$

where C_L is a non-dimensional lift coefficient. The value of C_L depends on the particular bubble size and it can be calculated as

function of non-dimensional variables such as the bubble Eötvös number and bubble Reynolds number [42]. In the present work, a constant value of 0.5 for C_L has been used, a value that has been proved to give accurate results in bubble columns with low aspect ratios [39].

The virtual mass force is proportional to relative phasic accelerations as follows:

$$\underline{F}_{lg}^{VM} = -\underline{F}_{gl}^{VM} = \alpha_g \rho_l C_{VM} \left(\frac{D_g \underline{v}_g}{D_t} - \frac{D_l \underline{v}_l}{D_t} \right) \quad (26)$$

The non-dimensional virtual mass coefficient takes the value of $C_{VM} = 0.5$ for inviscid flow around an isolated sphere.

3. Numerical model

The numerical solution of the continuity and momentum equations is obtained using the CFD code ANSYS CFX 10.0, which is a vertex-centered code based on the finite volume numerical method.

The Navier-Stokes conservation equations described above are discretized using an element-based finite volume method [43]. The mesh may consist of tetrahedral, prismatic, pyramid, or hexahedral elements. The discretization of the conservation equations is fully conservative and time-implicit. The conservation equations are integrated over each control volume, volume integrals are converted to surface integrals using Gauss' divergence theorem, and surface fluxes are evaluated in exactly the same manner at the two control volumes adjacent to an integration point.

The advection scheme used to evaluate the variable (ϕ_{ip}) in terms of neighboring vertex values (ϕ) is extremely important for the solution accuracy. It can be written as

$$\phi_{ip} = \phi_{up} + \beta \nabla \phi \Delta \bar{r} \quad (27)$$

ϕ_{up} is the upwind vertex value and Δr is the vector from the upwind vertex to the integration point. The quantity $\beta \nabla \phi \Delta \bar{r}$ is called numerical advection correction. If $\beta = 0$, this scheme recovers the first-order upwind scheme, which is bounded but excessively diffusive. If $\beta = 1$, this scheme is a second-order upwind-biased scheme, but unbounded. A bounded high-resolution scheme, used in this work, can be obtained by making β as close to 1 as possible, but reducing where necessary to prevent overshoots and undershoots from occurring. For standard advection terms, CFX uses a method similar to that described by Barth and Jesperson [44]. This numerical method is formally second order accurate as well as bounded since it reduces to first order only near discontinuities. Accuracy and stability are then assured, while non-physical numerical oscillations are avoided. This scheme is used for the continuity and momentum conservation equations while an upwind scheme is used for the k–ε turbulence equations. However, the numerical diffusion introduced by these equations has minor or no effect, as described by Oey [26]. The mass flows must be discretized carefully to avoid pressure–velocity decoupling. This is performed by generalizing the interpolation scheme proposed by Rhie and Chow [45]. The linear system of equations is solved using a coupled algebraic multigrid technique [46].

4. Experimental and computational procedures

4.1. Experimental set-up

The experimental set up includes a 0.2 m wide, 1.8 m high and 0.04 m deep PMMA (polymethyl methacrylate) bubble column. The column is filled with water ($H = 45$ cm) at room temperature and atmospheric pressure while air is fed from the gas chamber through an aluminum sparger (eight centered holes of 1 mm of diameter and 6 mm pitch). This column configuration has been proved to be very interesting since liquid vortices generated by the bubble plumes are a favorable factor for mixing and, therefore, for speeding up all transport processes [2]. Additionally, the existence of flow structures showing unsteady liquid recirculation is a typical phenomenon in industrial-scale bubble columns [1]. U_G is varied from 0.24 to 2.13 cm s^{-1} by means of the appropriate combination of volumetric flow meters. This range of values of U_G allows the study of different flow regimes [25]. Validation of the numerical simulations is based on three sets of experimental results:

1. Visual observations: qualitative validation of the numerical results is performed by means of the images obtained using a digital video system consisting on a digital camera and a 500 W halogen light.
2. Global gas hold-up and POP: quantitative validation of the numerical results is based on the pressure time series obtained by means of two piezo-resistive sensors (Keller PR35X, 0–200 and 0–500 mbar with and a resolution of 0.002% of the full scale) flush mounted on the sidewall of the column. The calculation of the global gas hold-up is based on the well-known manometric method that considers the static pressure difference between two pressure sensors [47,48]. On the other hand, the calculation of the mean POP is performed by means of the transformation of the pressure time series from the time domain to the frequency domain and the subsequent identification of the characteristic frequency of the peak in the low frequency band (0–1 Hz) [16].
3. Sauter mean bubble diameter: quantitative validation of the numerical results obtained from the multiple bubble size model is based on the experimental determination of the bubble size distribution. A video image system consisting on a high-speed digital camera (Redlake MotionScope PCI® 1000s) and a 500 W halogen light is used for such purpose. Several frames are selected for each value of U_G. After manipulation of the obtained frames by means of an image processing software, the Sauter mean bubble diameter (d_{32}) is calculated using Eq. (28):

$$(d_{32})_{experimental} = \frac{\sum_{i=1}^{k} n_i d_{Bi}^3}{\sum_{i=1}^{k} n_i d_{Bi}^2} \quad (28)$$

Further details about the experimental set-up and the calculations performed are given somewhere else [25,49].

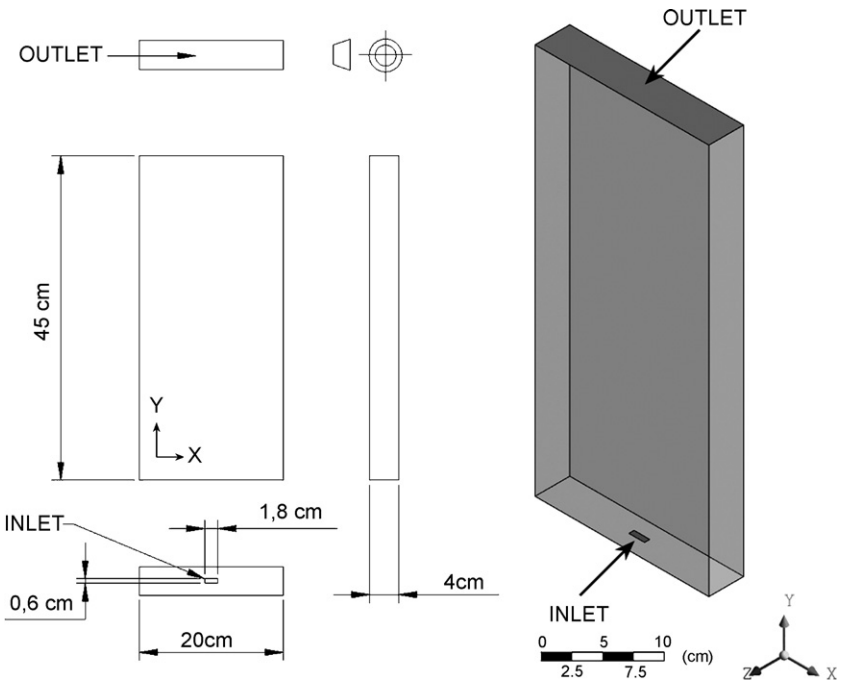

Fig. 1. Bubble column geometry. (a) Dimensions and (b) 3D representation.

4.2. Numerical solution

The simulated bubble column is shown in Fig. 1. A high resolution advection discretization scheme is used for the numerical solution of the model equations. In order to establish adequate spatial resolution, three different non-uniform hexahedral grids having 17 (width) × 7 (depth) × 25 (height) cells (coarse), 32 × 11 ×47 cells (medium) and 62 × 19 × 92 cells (fine) are used in this work (Fig. 2). Time integration is performed by means of a second order backward Euler time discretization

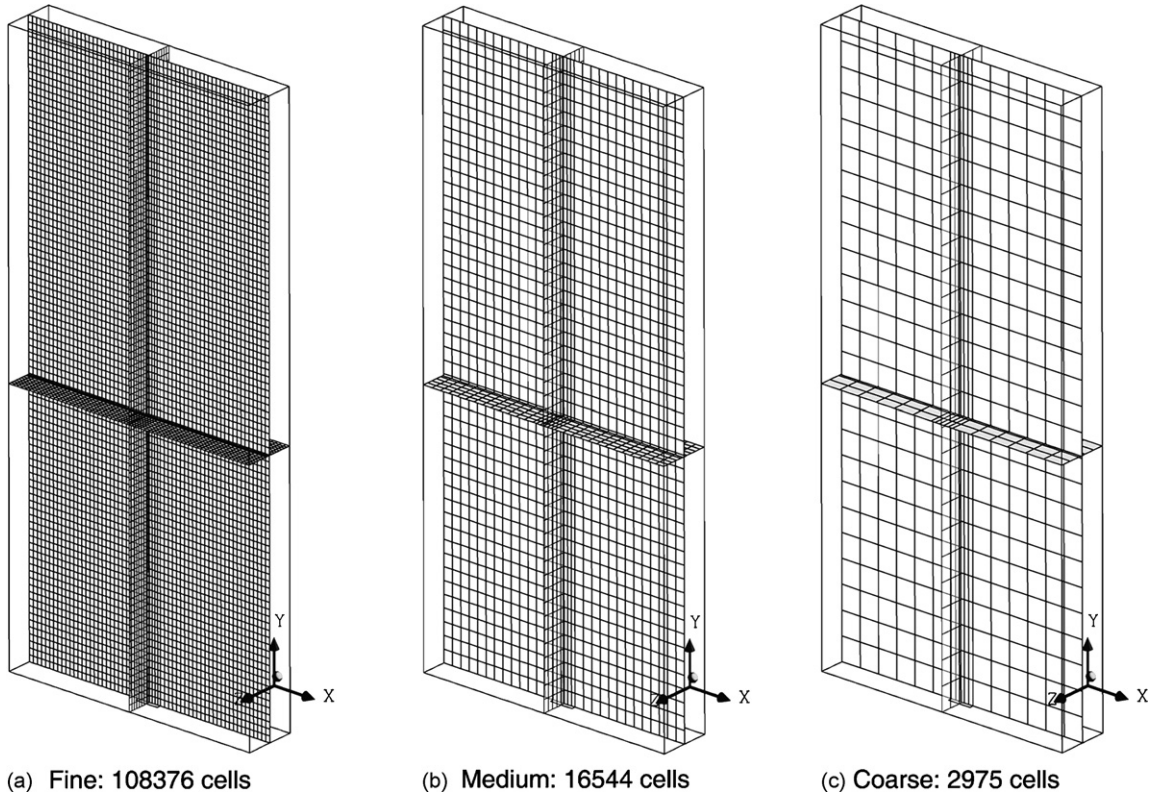

Fig. 2. Mesh configurations used in the numerical simulations. (a) Fine; (b) medium; (c) coarse.

scheme. The effect of changing the time step on the results is studied in order to prove the appropriateness of the selected time step.

The area of the sparger through which gas enters the domain is modeled as a rectangle with an area equal to the total area enclosed by the 8 centered 1 mm circular holes [8] (see Fig. 1). The gas inlet is modeled providing the value of the normal velocity as a function of the gas volumetric flow rate. Only bubbles of the fifth group (Table 1) are considered to enter the domain. At the gas outlet, a degassing boundary condition is implemented. This type of boundary condition is used to model a free surface from which dispersed bubbles, that "see" this boundary as an outlet, are permitted to escape, but the liquid phase, that "sees" it as a free-slip wall, is not. Outlet pressure is not specified, instead, a pressure distribution is computed on this fixed-position boundary, which can be interpreted as representing the weight of the surface height variations in the real flow. The height of the gas–liquid dispersion is considered equal to the height of the liquid phase at time zero. Considering that the maximum global gas hold-up experimentally observed in this work is approximately 4%, this approximation can be considered valid. At the rest of the walls, a no-slip boundary condition for the liquid phase and a free-slip boundary condition for the gas phase are considered.

Simulations are carried out on two computers powered by an AMD Athlon 64 3200+ processor running at 2.01 GHz with 2.00 Gb of RAM and an AMD Athlon 64 X2 4400+ Dualcore processor running at 2.21 GHz with 3.37 GB RAM, respectively. Transient simulations are started using the results of a steady state simulation. Each transient simulation takes from several hours to several days depending on the spatial and time resolution. Unless it is otherwise stated, the simulations are performed without the consideration of non-drag forces. The mesh and time-step used in the simulations are selected in the next section of this paper.

5. Results and discussion

5.1. Mesh size and time-step optimization

In order to keep under reasonable limits the computational time spent on the selection of the appropriate mesh and time step, the results presented in this section corresponds to a simplification of the multiple bubble size model described in Table 1. This simplification consists on the reduction of the number of bubble groups to 5 instead of 10, keeping the same maximum and minimum diameters. This simplification is only applicable to this section.

As it was mention above, in order to study the influence of the mesh resolution on the results, three different grids have been generated: coarse, medium and fine (Fig. 2). The results are presented in Table 2 for a time step of 0.025 s and $U_G = 2.13$ cm/s. As it can be observed, a better agreement between experimental and numerical results is achieved with the coarse mesh, whereas numerical results with medium and fine grids differ more from experimental data. Buwa et al. [16] and Pfleger and Becker [22] also reported that as the grid size is decreased, the agreement between predicted long time-averaged axial velocity and experimental data deteriorates. Bech [4] found that transient turbulence models produce new modes of instability in the plume oscillation as the mesh is refined, thus being the results dependent on which length scales of motion are represented. This fact was associated with the turbulent spectrum. In his work [4] a comparison between the Kolmogorov length scale and the cell size is also shown. It was found that meshes with cell size around 50–100% of the Kolmogorov length scale produced similar or grid-independent results, which were in good agreement with experimental data. However, for finer meshes with cell size around 20% of the Kolmogorov length scale, new modes of oscillation occurred. Other authors like Frank [50] and Krepper et al. [50] mention that the specification of the spatial resolution may be restricted by the bubble size. Krepper [51] also cites the works of Milelli [52] and Lakehal et al. [53], who recommend a cell size larger than 1.5 times the bubble size for LES simulations. Considering the results presented in Table 2, the coarse mesh has been selected for the further work unless otherwise indicated, as it provides better agreement with experimental results. A more detailed research on the relative importance of numerical errors and model errors is necessary in order to determine the reason for this fact, as finer meshes are assumed to be more accurate in terms of the size of the truncation error.

Table 2
Mesh size effect on the calculated gas hold-up and plume oscillation period parameters

Mesh	Number of cells	Number of nodes	Cell size (mm)	Gas hold-up	POP (s)
Coarse	2975	3744	11.2	0.0430	2.84
Medium	16544	19008	6.0	0.0370	3.42
Fine	108376	117180	3.2	0.0366	3.20

Time step: 0.025 s; U_G: 0.0213 m/s; experimental gas hold-up = 0.041; experimental POP = 2.80 s; calculated mean Sauter diameter = 5.26 mm.

The influence of the time-step size on the results has been also investigated. The size of the time step is related to the grid size via the CFL number. To resolve the transient phenomena, a CFL number of the order of one is required [4]. In this way, the time step can be selected based on the CFL condition:

$$\Delta t \leq \frac{\Delta y}{|v|} \tag{29}$$

where $|v|$ is the magnitude of the vertical component of the velocity vector, Δy is the characteristic dimension of the cell and Δt the time step. Considering the characteristic dimension of the cells in the coarse mesh and a conservative value for the terminal rise velocity of large bubbles of 30 cm/s, the application of the CFL criterion leads to a value of the time step of $\Delta t \leq 0.037$ s. Finally, based on the results shown in Table 3, the time step was selected to be 0.025 s. On one hand, $\Delta t = 0.025$ s verifies the CFL condition and, on the other hand, further refining of the time step does not lead to significant changes on the predicted results.

Table 3
Time-step effect on the calculated gas hold-up and plume oscillation period parameters

Time step (s)	Gas hold-up	POP (s)
0.25	0.0430	3.20
0.025	0.0430	2.84
0.01	0.0463	2.83

Mesh: coarse; U_G: 0.0213 m/s; experimental gas hold-up = 0.041; experimental POP = 2.80 s.

5.2. Flow visualization: experimental versus simulated results

Fig. 3(a) shows characteristic experimental snapshots of the vortical flow in the bubble column at different U_G values. Additionally, Fig. 3(b) shows the simulation results: gas hold-up distribution and water superficial velocity. It can be clearly seen that experimental and calculated results are in good agreement regarding basically the existence of the three-region vortical flow with several particularities that depend on the values of U_G. The calculated results reproduce accurately the central bubble plume (central bubble plume region) that moves periodically from side to side of the bubble column with decreasing period and increasing amplitude as U_G increases. The vortical region is also reproduced, with three transient circulation cells of variable dimensions. The liquid phase, which does not escape from the bubble column, descends along the sidewalls of the bubble column (descending flow region). The calculated dispersion of the bubbles at different U_G values is, as well, in good accord with the experimental observations. At the lowest U_G studied, there are no bubbles outside the central bubble plume region. Close to the sparger, the bubbles gather together, while close to the liquid level, the bubbles spread, covering a wider length of the bubble column width. However, partial aeration in the whole bubble column is clear. As U_G is increased up to 1.20 cm/s, small bubbles are trapped by the moving liquid vortices in the higher section of the bubble column and they move downwards along the sidewalls. Therefore, total aeration is now obtained in the higher section of the bubble column. At the maximum U_G value, the downward movement of the liquid draws bubbles to a region close to the gas inlet resulting in the total aeration of a great part of the bubble column.

It is also interesting to point out the significant differences between the instantaneous flow regime experimentally observed and accurately reproduced by the simulations and the time-average flow regime obtained when time-averaged experimental parameters (such as gas hold-up or liquid velocity) are used. Fig. 4 illustrates these differences. It can be observed that the resulting time-averaged flow pattern consists on a non-uniform velocity distribution presenting an upward flow in the column center and a downward flow along the column walls, a liquid circulation mode, commonly referred as "Gulf-stream" or "Cooling tower" flow regime [17]. This type of flow differs considerably from the instantaneous flow pattern previously described. It is therefore essential to capture the dynamic nature of the flow to accurately describe the hydrodynamics as well as mixing and transfer processes in bubble columns.

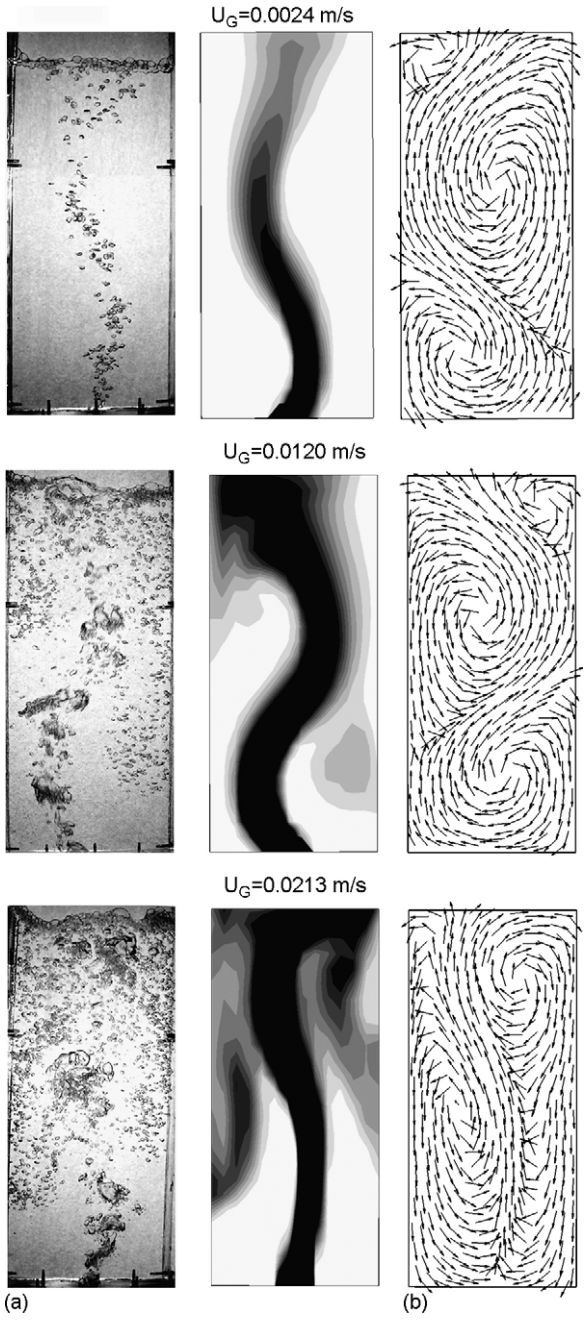

Fig. 3. Snapshots of the gas–liquid flow in the bubble column at different values of U_G. (a) Experimental; (b) computational. From left to right: gas hold-up distribution represented by 10 contours 0 (white); >0.1 (black). Water superficial velocity field (normalized arrows).

5.3. Gas hold-up and POP: experimental versus simulated results

The gas hold-up is a very important variable in the study of bubble columns. The analysis of the evolution of the global gas hold-up with U_G is a basic procedure on the flow regime identification under particular experimental conditions [54,55]. Global gas hold-up data measured and calculated are shown in Fig. 5. As it can be readily seen, there is no change in the slope of the curve described by the experimental results and a continuously

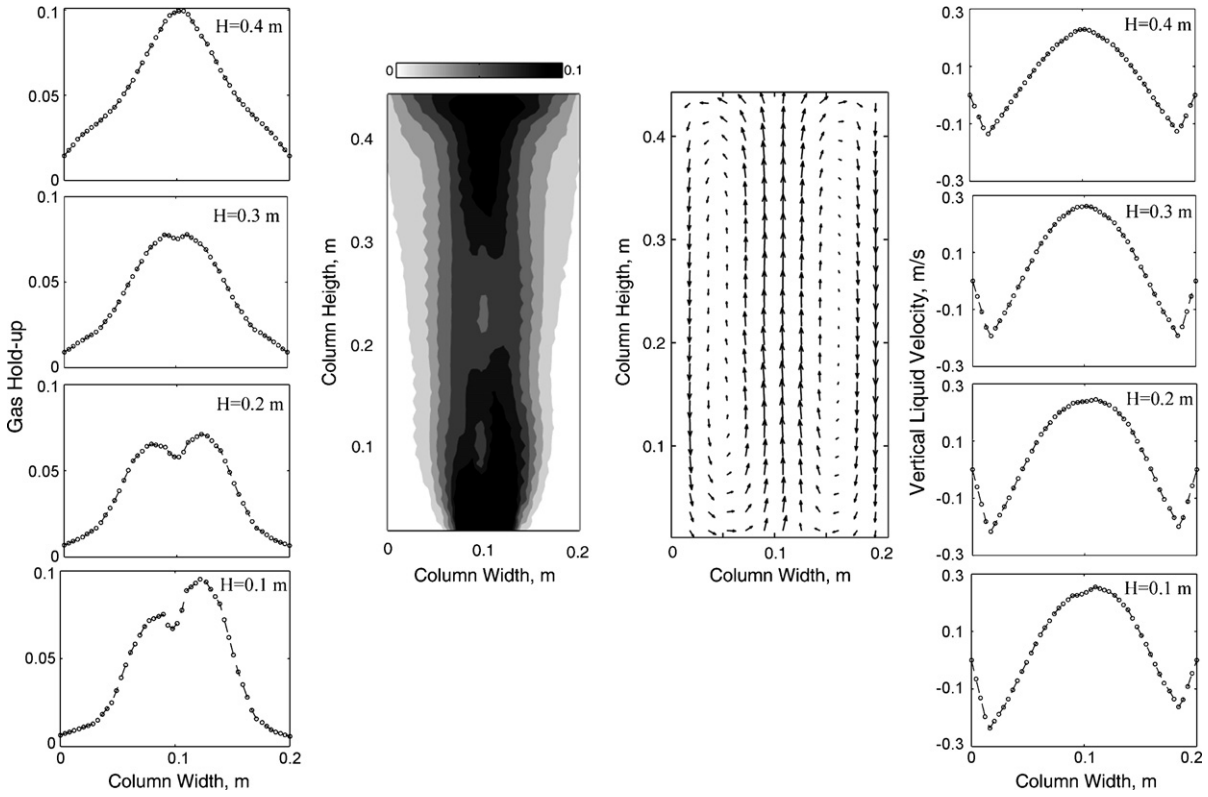

Fig. 4. Time averaged gas hold-up and vertical liquid velocity at $U_G = 0.0120$ m/s, $z = 0.02$ m. From left to right: time averaged gas hold-up profiles at different bubble column heights (y); time averaged gas hold-up distribution represented by contours; time averaged vertical liquid velocity field represented by arrows (maximum velocity: 0.294 m/s; minimum velocity: 0.0288 m/s); time averaged vertical liquid velocity profiles at different bubble column heights (y).

increasing concave line represents well the global hold-up data. These features of the curve point to the existence of a unique flow regime that, according to the flow images, corresponds to the vortical flow. Good agreement is obtained between the experimental data and the simulations performed, what confirms the choice of the bubble size distribution as well as the numerical model.

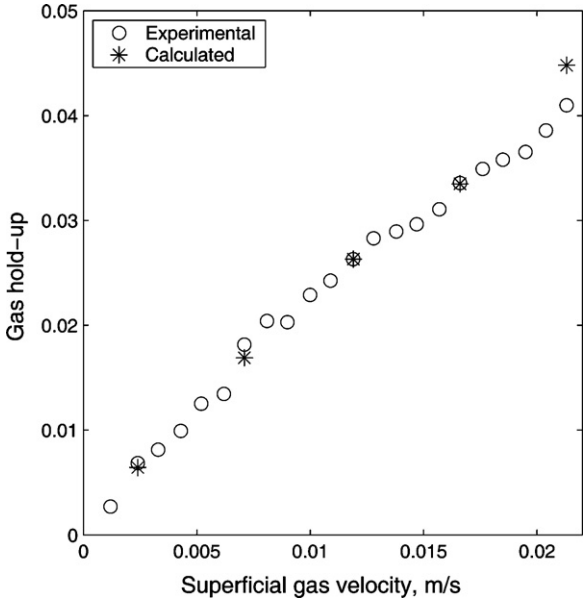

Fig. 5. Comparison between experimental and calculated global gas hold-up at different superficial gas velocities.

Most of the problems encountered when calculating the hold-up take place at high U_G values, basically due to the common assumption of single bubble size distribution [56]. However, considering that most industrial applications of bubble columns are based on the turbulent flow regime and, therefore, take place at high U_G values, it is obvious that the introduction of multiple bubble size simulations is essential. Nevertheless, in some cases, the introduction of multiple bubble sizes does not solve the problem completely [35] and the model underestimates the value of gas hold-up at low U_G values while it overestimates it at high U_G values, not being able to account for the changes in the flow regime. In the cases presented here, the vortical regime prevails and even though differences in bubble distributions are clearly observed at different U_G, the multiple bubble size model seems to perform well under all experimental conditions studied in this work that include higher U_G values than those presented by other authors [3,5,16].

The wavelike motion of the bubble plumes is an essential characteristic of partially aerated 2D bubble columns as it has been shown in the previous section. Here, a quantitative validation of the numerical model used in the simulation based on plume oscillation experimental data is presented. Time series of simulated horizontal liquid velocities at different U_G values are shown in Fig. 6. The periodicity of the movement of the bubble plume can be clearly observed at U_G values up to 1.66 cm/s. At $U_G = 2.13$ cm/s the velocity time series does not appear to be periodic and several other physical processes with different characteristic frequencies seem to be affecting this parameter.

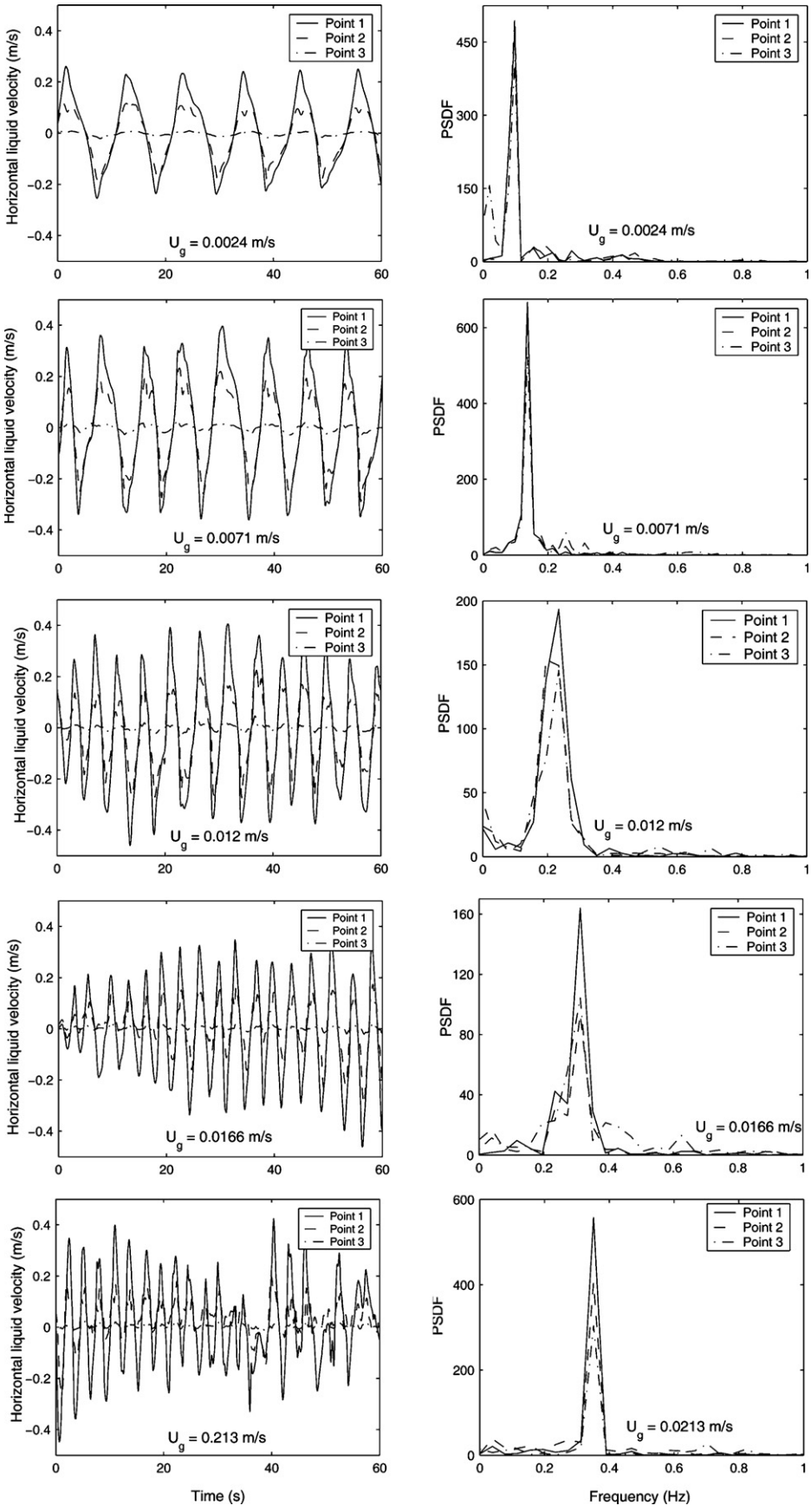

Fig. 6. Calculated horizontal liquid velocity and corresponding power spectral density function at different superficial gas velocities. Point 1: $x = 0.1$ m, $y = 0.225$ m, $z = 0.02$ m; point 2: $x = 0.05$ m, $y = 0.225$ m, $z = 0.02$ m; point 3: $x = 0.005$ m, $y = 0.225$ m, $z = 0.02$ m.

This is probably due to the existence of a wider bubble size distribution caused by the coalescence and breakup of bubbles that leads to the existence of small bubbles that oscillate much more chaotically and irregularly [16]. Another important factor might be the omission of the non-drag forces on the numerical model. As it will be shown later, the consideration of lift forces on the simulations leads to a much more periodic horizontal liquid velocity at high U_G values. However, lift forces affect other parameters resulting in higher POP, higher global gas hold-up and non-symmetric oscillation of the plume. This is discussed in detail in section 5.5. Also, in Fig. 6 it can be seen the differences on the amplitudes of the waves described by the horizontal liquid velocity characteristic of bubble plumes. While at the lowest U_G value studied here the horizontal liquid velocity oscillates between ±0.2 m/s, this amplitude increases to values up to 0.4 m/s at intermediate volumetric gas flows. These values agree well with those presented by other authors [5,16] at similar values of U_G.

The calculation of the POP was based on the number of cycles displayed by the horizontal liquid velocity profile on a given period of time measured at the central point of the bubble column (Fig. 6) [16]. This method gives accurate results at low U_G values. However, as U_G is increased, the number of cycles cannot be counted so accurately. In these cases, the horizontal velocity data was normalized and the resulting data set is transformed from the time domain to the frequency domain by means of the calculation of the fast Fourier transform [57]. The results are shown in Fig. 6. As it can be seen, the characteristic peak clearly moves to higher values of frequency as U_G is increased. The POP is now calculated as the inverse of the characteristic frequency obtained in the power spectrum. The results are shown in Fig. 7. Good agreement between the experimental and the calculated values of the bubble plume oscillation period is obtained. At low U_G values, the frequency of oscillation is low and it rapidly increases as U_G increases until reaching an approximately constant value at high U_G values. This variation has been related to the bubble size distribution inside the bubble column [16]. The occurrence of the coalescence and break-up processes increases rapidly at low values of U_G while they reach an approximately steady level of occurrence at high values of U_G.

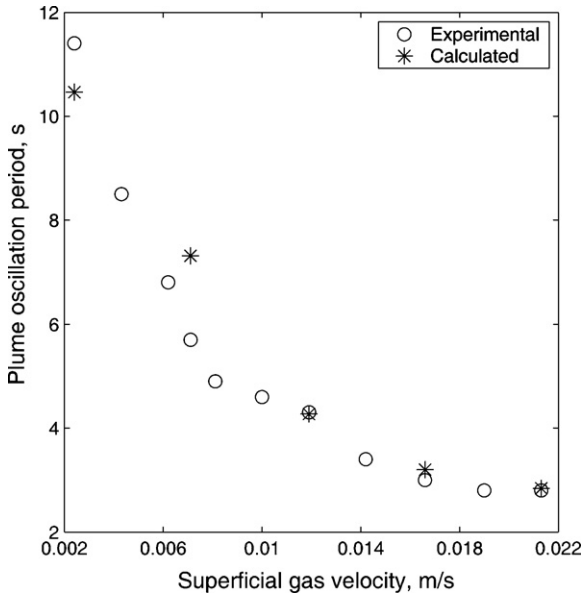

Fig. 7. Comparison between experimental and calculated POP at different superficial gas velocities.

5.4. Bubble size distribution: experimental versus simulated results

Only a few publications have dealt with U_G values at which coalescence and break-up processes are important. However, this is an essential phenomenon on flow regime transitions in bubble columns and becomes predominant at high U_G values that result in the existence of the turbulence flow regime. In this work, as it has been previously pointed out, the bubble column works under the vortical flow regime at all the studied values of U_G. However, it is observed that the bubble size distribution evolves from a single size to a multiple size mode. Therefore, it seems clear that the modeling of the bubble column should allow the possibility of the existence of several bubble sizes. In this section, results obtained from single and multiple size bubble groups models are compared with experimental data. Additionally, the experimental and theoretical mean Sauter diameters are presented.

Tables 4 and 5 show the results obtained when using mono and multiple bubble size models. The former model was based on bubbles of 5 mm diameter. Acceptable agreement between calculated (both single and multiple size bubble distributions) and experimental gas hold-up and POP is obtained. Nevertheless, as it can be seen, the monodispersed model leads, in most of the cases, to greater relative errors than those obtained with the polydispersed model and therefore, the use of the latter model improves the prediction of both the global gas hold-up and of the POP, which are the parameters used to described the hydrodynamics in the bubble column.

Table 4
Comparison of experimental and calculated gas hold-up obtained using monodispersed (M) and polydispersed (P) models

U_G (m/s)	Gas hold-up			Relative error	
	Experimental	Simulated (M)	Simulated (P)	Experimental–simulated (M)	Experimental–simulated (P)
0.0024	0.0069	0.0064	0.0064	7.81	7.81
0.0071	0.0181	0.0164	0.0169	10.37	7.10
0.0120	0.0263	0.0221	0.0263	19.00	0.00
0.0166	0.0336	0.0322	0.0335	4.35	0.30
0.0213	0.0410	0.0443	0.0448	7.45	8.48

Table 5
Comparison of the experimental and calculated plume oscillation period (POP) obtained using monodispersed (M) and polydispersed (P) models

U_G (m/s)	POP (s)			Relative error	
	Experimental	Simulated (M)	Simulated (P)	Experimental–simulated (M)	Experimental–simulated (P)
0.0024	11.38	10.85	10.46	4.88	8.80
0.0071	5.69	7.02	7.31	18.95	22.16
0.0120	4.3	4.39	4.27	2.05	0.70
0.0166	3.0	3.66	3.20	18.03	6.25
0.0213	2.8	3.06	2.84	8.50	1.41

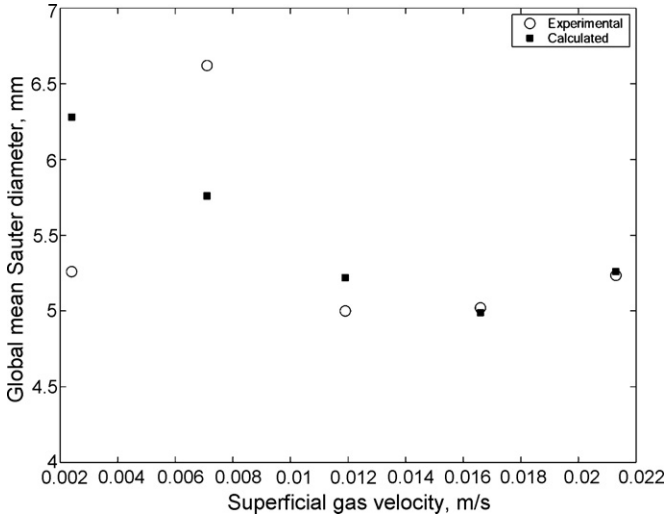

Fig. 8. Comparison between experimental and calculated global mean Sauter diameter.

The calculation of the global mean Sauter diameter obtained from the simulations is based on Eq. (30) [35]:

$$(d_{23})_{\text{calculated}} = \frac{1}{\sum_{i=1}^{10}(F_i/d_i)} \tag{30}$$

F_i and d_i are the global mean size fraction and diameter of group i, respectively. The comparison between experimental and calculated mean Sauter diameter at different U_G values is presented in Fig. 8. The prediction of the mean Sauter diameter by means of the CFD calculations is satisfactory except maybe the calculations that correspond to $U_G = 0.24$ and 0.71 cm/s, condition at which the model over and under predicts the experimental values, respectively. Fig. 8 also shows the evolution of the mean Sauter diameter with U_G. The study of this type of graphs is very important since they are illustrative of the existing flow regime [35,58]. In the plot obtained in this work two regions can be distinguished. First, at low U_G values, the mean Sauter diameter increases until reaching a maximum value. Following this maximum, the Sauter diameter decreases to become, in the region of $U_G = 1.19$ cm/s, approximately constant. The evolution of the mean Sauter diameter is directly related to the coalescence and break-up phenomena. At low U_G values, the coalescence of bubbles predominates with the consequent increase on the mean Sauter diameter. As U_G increases, the break-up phenomena starts being significant until becoming equivalent to the level of occurrence of coalescence, velocity at which the mean Sauter diameter does not change significantly. This region of constancy of the mean Sauter diameter is characteristic of the transition and heterogeneous regime [58] and, in the case presented here, is denoting the transition to the FDVF.

5.5. The role of lift and virtual mass forces

In order to study the influence of the non-drag forces, the following cases are studied:

- Case A: a first set of calculations considering only the drag force.
- Case B: a second set of calculations where drag and virtual mass forces are considered.
- Case C: a third set of calculations with drag and lift forces.

This strategy is followed for two different values of U_G, and the results are shown in Table 6. Wall force is not considered in

Table 6
Comparison of the experimental and calculated gas hold-up and plume oscillation period for $U_G = 0.0024$ and 0.0213 m/s

Case	U_G (m/s)	Gas hold-up		Plume oscillation period (s)	
		Experimental	Calculated	Experimental	Simulated
A	0.0024	0.0069	0.0064	11.378	10.460
B			0.0063		10.332
C			0.0070		11.660
A	0.0213	0.041	0.0448	2.80	2.84
B			0.0403		2.84
C			0.0876		3.47

Case A: just drag force; case B: drag and virtual mass forces; case C: drag and lift forces.

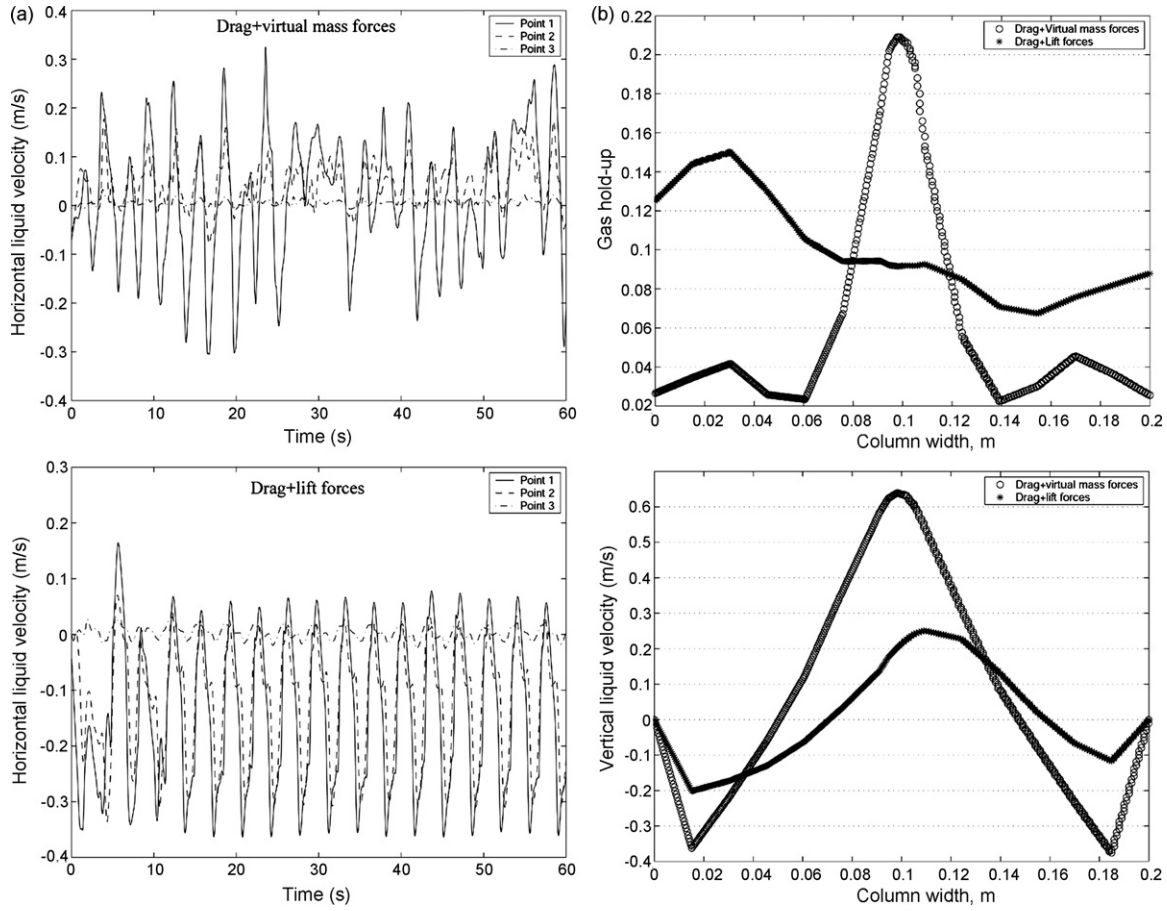

Fig. 9. (a) Predicted variation of the horizontal liquid velocity with time. Point 1: $x = 0.1$ m, $y = 0.225$ m, $z = 0.02$ m; point 2: $x = 0.05$ m, $y = 0.225$ m, $z = 0.02$ m; point 3: $x = 0.005$ m, $y = 0.225$ m, $z = 0.02$ m. (b) Time averaged hold-up and vertical liquid velocity at $y = 0.225$ m, $z = 0.02$ m. $U_G = 0.0213$ m/s.

any of the studies of this work given the small vertical dimension of the bubble column.

As it can be seen in Table 6, for low U_G values, the addition of lift forces improves the prediction of the experimental gas hold-up and POP results. However, for high U_G values, case C over-predicts both simulated hold-up and POP. In fact, this is the case where lift forces have a more important contribution, as higher U_G yield higher continuous phase shear rates. Therefore, cases with lower superficial velocities are expected to present fewer differences, as confirmed by the results shown in Table 6. Additionally, it is observed that the values of simulated POP are not very sensitive to the virtual mass force term, as it has been also reported by Buwa et al. [16]. In fact, for the range of U_G values considered in this work, results with only drag forces and with drag and virtual mass forces are in the same order of accuracy, with relative errors in the prediction of gas hold-up and POP of less than 10%. The reason is that the relative phasic acceleration, which is responsible for the virtual mass force, is small for the range of U_G values considered. Therefore, the contribution of virtual mass force is not dramatic. These results contrast with those reported by other authors [12] that show improved agreement between experimental and numerical POP values when virtual mass force was included.

Additionally to the studied numerical values of the gas hold-up and the POP, the evolution of the horizontal liquid velocity with time and the time averaged gas hold-up and vertical liquid velocity are studied. While at $U_G = 0.24$ cm/s there are no significant differences between cases A, B and C, at $U_G = 2.13$ cm/s, case C shows some particularities. Fig. 9 shows a comparison of the parameters mentioned above for cases B and C (case A and B are equivalent) at $U_G = 2.13$ cm/s. As it can be clearly seen in Fig. 9 (a), the time evolution of the horizontal liquid velocity at three different positions for cases B and C differ considerably. While for case B, the horizontal liquid velocity fluctuates up and down in an apparent non-periodic way, the same variable shows a clear periodicity and asymmetry with respect to zero for case C. These differences are evidenced in Fig. 9 (b), that shows the time averaged gas hold-up and vertical liquid velocity at $y = 0.225$ m, $z = 0.02$ m for cases B and C. As it can be readily observed, the time averaged profiles of gas hold-up and vertical liquid velocity for case B are typical of the "cooling tower" flow regime previously described, characteristic of the coalesced flow regime and experimentally observed by other authors [5,16]. However, for case C, the profiles are not symmetric with respect to the center of the column width, especially the gas hold-up profile. This results in a time-averaged flow regime (Fig. 10) showing a central meandering bubble plume characteristic of the instantaneous flow regime. The results obtained for case C show how the lift force cause, at least temporarily, the bubble plume to move preferably to one side of the bubble column. This is due to the

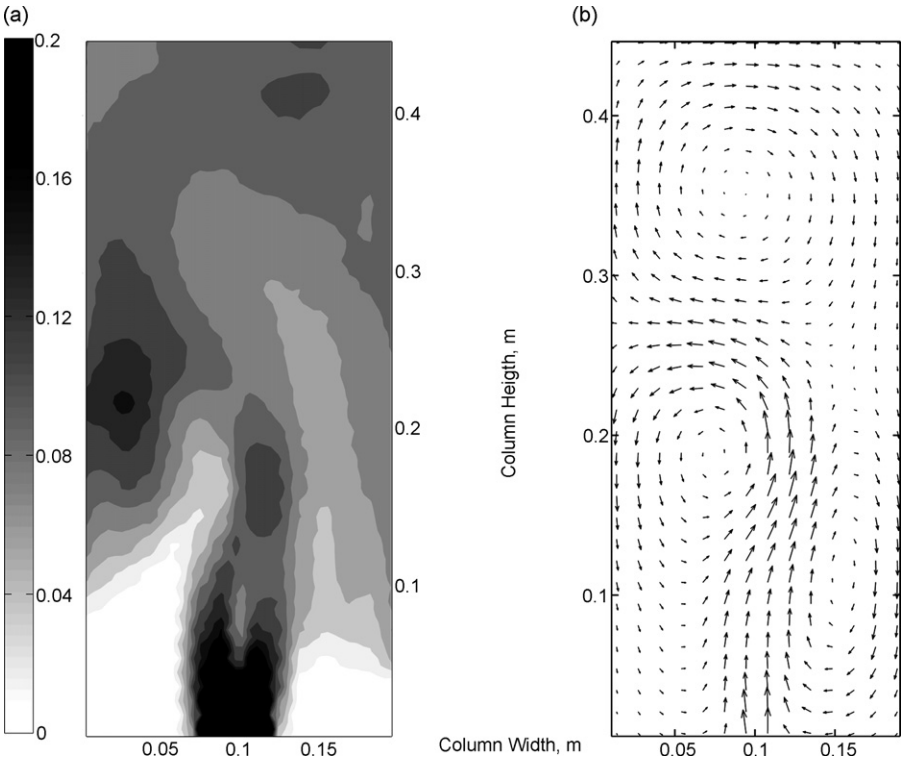

Fig. 10. Time averaged gas hold-up distribution represented by contours (a) and time averaged vertical liquid velocity field represented by arrows (maximum velocity: 0.433 m/s; minimum velocity: 0.013 m/s) (b) at $U_G = 0.0213$ m/s. The results correspond to case C.

fact that the lift force acts perpendicular to the direction of relative motion of the two phases (as shown in Eq. (13)) and causes the bubbles to move towards the sides. However, since experimental results differ considerably from the simulated results, either the inclusion of the lift force in this type of experimental studies is not adequate, or the lift coefficient is not appropriate.

6. Summary and conclusions

Dynamics of the gas–liquid flow in a rectangular bubble column have been studied by means of E–E simulations. The reference model has considered a multiple bubble size distribution, consisting on 10 groups of bubbles of minimum and maximum diameters of 1 and 10 mm, respectively, and only the drag force in the interphase momentum exchange. Qualitative validation of the proposed model has been based on processed images of the gas–liquid flow in the bubble column. Quantitative validation has been based on the comparison between experimental and simulated results of three essential parameters in the hydrodynamics of this type of two-phase flow: the global gas hold-up (obtained by means of the manometric method), the POP (obtained form wall pressure fluctuations time series) and the bubble size distribution (obtained by photography). In order to study other alternatives to the reference model described above, two modifications have been introduced. First, the multiple bubble size has been substituted by a single bubble size distribution and the results have been compared. Second, non-drag forces (virtual mass and lift forces) have been included and, again, the results have been compared to the reference model. Previous studies on the influence of mesh resolution and time step have been performed in order to establish the proper grid and time step for the simulations.

The results presented in this paper reveal that, qualitatively, the model reproduces the type of gas–liquid flow observed in the bubble column, that is, the three-region vortical flow. The model predicts the descending, vortical and central bubble plume regions as well as the oscillating movement of the plume that were distinguished visually. Additionally, the experimentally observed evolution of the aeration in the bubble column with U_G is in good accord with the calculated results. Quantitatively, both global gas hold-up and POP are fairly well reproduced by the simulations with relative errors (in absolute value) that oscillate between 0–9 and 0–22%, respectively. When the results obtained with a multiple size distribution model are compared with the results obtained using single bubble size distribution, it can be said that most of the global gas hold-up and POP predictions obtained with the later model result in larger relative errors, especially at higher values of U_G. However, at the lower superficial gas velocities ($U_G = 0.24$ and 0.71 cm/s), precisely when coalescence and break-up phenomena are less important, the monodispersed model generates POP values closer to experimental data. The experimental results obtained for the global mean Sauter diameter reveal the existence of a superficial gas velocity ($U_G \approx 1.20$ cm/s) that separates two regions: one region at which coalescence predominates (at low U_G) and a second region at which the frequency of occurrence of coalescence and break-up phenomena are leveled. The Sauter diameter obtained by means of the simulations is in good agreement with the experimental results at values of U_G of 1.20 cm/s and up. At lower values of U_G, the agreement between experimental and

calculated data becomes poorer and therefore, the break-up and coalescence models used in these simulations are not able to reproduce accurately the frequency of occurrence of these phenomena. The consideration of non-drag forces resulted in two different conclusions. The virtual mass force does not have a considerable effect on the results at any of the studied values of U_G while the lift force has remarkable negative effects on the calculated parameters at the highest values of U_G, at which it is considered to have the greatest effect. The calculated global gas hold-up and POP as well as the time-averaged and time dependent results differ considerably from the experimental results. Different lift force coefficients may be used in future studies to determine the adequate values at particular values of U_G and bubble size.

Acknowledgements

This research was performed under a grant from the Ministerio de Educación y Ciencia (Spain), CTQ2005-01395/PPQ.

References

[1] A. Sokolichin, G. Eigenberger, Applicability of the standard k–ε turbulence model to the dynamic simulation of bubble columns. Part I. Detailed numerical simulations, Chem. Eng. Sci. 54 (1999) 2273–2284.
[2] V.V. Buwa, V.V. Ranade, Characterization of dynamics of gas–liquid flows in rectangular bubble columns, AIChE J. 50 (2004) 2394–2407.
[3] O. Borchers, C. Busch, A. Sokolichin, G. Eigenberger, Applicability of the standard k–epsilon turbulence model to the dynamic simulation of bubble columns. Part II. Comparison of detailed experiments and flow simulations, Chem. Eng. Sci. 54 (1999) 5927–5935.
[4] K. Bech, Dynamic simulation of a 2D bubble column, Chem. Eng. Sci. 60 (2005) 5294–5304.
[5] D. Pfleger, S. Gomes, N. Gilbert, H.-G. Wagner, Hydrodynamic simulations of laboratory scale bubble columns fundamental studies of the Eulerian–Eulerian modelling approach, Chem. Eng. Sci. 54 (1999) 5091–5099.
[6] R. Krishna, J.M. van Baten, M.I. Urseanu, Three-phase Eulerian simulations of bubble column reactors operating in the churn-turbulent regime: a scale up strategy, Chem. Eng. Sci. 55 (2000) 3275–3286.
[7] Y. Pan, M.P. Dudukovic, M. Chang, Dynamic simulation of bubbly flow in bubble columns, Chem. Eng. Sci. 54 (1999) 2481–2489.
[8] V.V. Buwa, D.S. Deo, V.V. Ranade, Eulerian–Lagrangian simulations of unsteady gas–liquid flows in bubble columns, Int. J. Multiphase Flow 32 (2006) 864–885.
[9] E. Delnoij, F.A. Lammers, J.A.M. Kuipers, W.P.M. van Swaaij, Dynamic simulation of dispersed gas–liquid two-phase flow using a discrete bubble model, Chem. Eng. Sci. 52 (1997) 1429–1458.
[10] D. Darmana, N.G. Deen, J.A.M. Kuipers, Detailed modeling of hydrodynamics, mass transfer and chemical reactions in a bubble column using a discrete bubble model, Chem. Eng. Sci. 60 (2005) 3383–3404.
[11] A. Lapin, A. Lobbert, Numerical simulation of the dynamics of two-phase gas–liquid flows in bubble columns, Chem. Eng. Sci. 49 (1994) 3661–3674.
[12] R.F. Mudde, O. Simonin, Two- and three-dimensional simulations of a bubble plume using a two-fluid model, Chem. Eng. Sci. 54 (1999) 5061–5069.
[13] E.I.V. van den Hengel, N.G. Deen, J.A.M. Kuipers, Application of coalescence and breakup models in a discrete bubble model for bubble columns, Ind. Eng. Chem. Res. 44 (2005) 5233–5245.
[14] A. Sokolichin, G. Eigenberger, A. Lapin, A. Liibbert, Dynamic numerical simulation of gas–liquid two-phase flows Euler/Euler versus Euler/Lagrange, Chem. Eng. Sci. 52 (1997) 611–626.
[15] S. Becker, A. Sokolichin, G. Eigenberger, Gas–liquid flow in bubble columns and loop reactors. Part II. Comparison of detailed experiments and flow simulations, Chem. Eng. Sci. 49 (1994) 5747–5762.
[16] V.V. Buwa, V.V. Ranade, Dynamics of gas–liquid flow in a rectangular bubble column: experiments and single/multi-group CFD simulations, Chem. Eng. Sci. 57 (2002) 4715–4736.
[17] J.J.J. Chen, M. Jamialahmadi, S.M. Li, Effect of liquid depth on circulation in bubble columns: a visual study, Chem. Eng. Res. Design 67 (1989) 203–207.
[18] J.-W. Tzeng, R.C. Chen, L.-S. Fan, Visualization of flow characteristics in a 2-D bubble column and three-phase fluidized bed, AIChE J. 39 (1993) 733–744.
[19] R.C. Chen, J. Reese, L.-S. Fan, Flow structure in a three-dimensional bubble column and three-phase fluidized bed, AIChE J. 40 (1994) 1093–1104.
[20] E. Delnoij, J.A.M. Kuipers, W.P.M. van Swaaij, Dynamic simulation of gas–liquid two phase flow: effect of column aspect ratio on the flow structure, Chem. Eng. Sci. 52 (1997) 3759–3772.
[21] S. Becker, H. De Bie, J. Sweeney, Dynamic flow behavior in bubble columns, Chem. Eng. Sci. 54 (1999) 4929–4935.
[22] D. Pfleger, S. Becker, Modelling and simulation of the dynamic flow behavior in a bubble column, Chem. Eng. Sci. 56 (2001) 1737–1747.
[23] J. Rensen, V. Roig, Experimental study of the unsteady structure of a confined bubble plume, Int. J. Multiphase Flow 27 (2001) 1431–1449.
[24] C. Vial, R. Laine, S. Poncin, N. Midoux, G. Wild, Influence of gas distribution and regime transitions on liquid velocity and turbulence in a 3-D bubble column, Chem. Eng. Sci. 56 (2001) 1085–1093.
[25] M.E. Diaz, F.J. Montes, M.A. Galán, Experimental study of the transition between unsteady flow regimes in a partially aereated 2D bubble column, Chem. Eng. Process., in press.
[26] R.S. Oey, R.F. Mudde, H.E.A. van den Akker, Sensitivity study on interfacial closure laws in two-fluid bubbly flow simulations, AIChE J. 49 (2003) 1621–1636.
[27] M.J. Prince, H.W. Blanch, Bubble coalescence and break-up in air-sparged bubble-columns, AIChE J. 36 (1990) 1485–1499.
[28] H. Luo, H.F. Svendsen, Theoretical model for drop and bubble breakup in turbulent dispersions, AIChE J. 42 (1996) 1225–1233.
[29] C.H. Lee, E.L.E., G.L.A., Bubble breakup and coalescence in turbulent gas–liquid dispersions, Chem. Eng. Commun. 59 (1987) 65–84.
[30] S. Lo, Application of population balance to CFD modelling of bubble flow via the MUSIG model, AEA Technol. AEAT-1096 (1996).
[31] P.M. Carrica, D. Drew, F. Bonetto, R.T. Lahey, A polydisperse model for bubbly two-phase flow around surface ship, Int. J. Multiphase Flow 25 (1999) 257–305.
[32] F. Lehr, D. Mewes, A transport equation for the interfacial area density applied to bubble columns, Chem. Eng. Sci. 56 (2001) 1159–1166.
[33] P. Chen, J. Sanyalb, M.P. Dudukovica, CFD modeling of bubble columns flows: implementation of population balance, Chem. Eng. Sci. 59 (2004) 5201–5207.
[34] P. Chen, M.P. Dudukovic, Three-dimensional simulation of bubble column flows with bubble coalescence and breakup, AIChE J. 51 (2005) 696–712.
[35] E. Olmos, C. Gentric, C. Vial, G. Wild, N. Midoux, Numerical simulation of multiphase flow in bubble column reactors. Influence of bubble coalescence and break-up, Chem. Eng. Sci. 56 (2001) 6359–6365.
[36] D.C. Wilcox, Turbulence Modeling for CFD, DCW Industries, 1998.
[37] B. Launder, D. Spalding, Lectures in Mathematical Models for Turbulence, Academic Press, 1972.
[38] A. Sokolichin, G. Eigenberger, Gas–liquid flow in bubble columns and loop reactors. Part I. Detailed modelling and numerical simulation, Chem. Eng. Sci. 49 (1994) 5735–5746.
[39] D. Zhang, N.G. Deen, J.A.M. Kuipers, Numerical simulation of the dynamic flow behavior in a bubble column: a study of closures for turbulence and interface forces, Chem. Eng. Sci. 61 (2006) 7593–7608.
[40] H.A. Jakobsen, B.H. Sannaes, S. Grevskott, H.F. Svedsen, Modelling of vertical bubble-driven flow, Ind. Eng. Chem. Res. 36 (1997) 4052–4074.
[41] J.R. Grace, T. Wairegi, T.H. Nguyen, Shapes and velocities of single drops and bubbles moving freely through immiscible liquids, Trans. Inst. Chem. Eng. 54 (1976) 167–173.
[42] A. Tomiyama, A. Sou, I. Zun, N. Kanami, T. Sakaguchi, Effects of Eötvös number and dimensionless liquid volumetric flux on lateral motion of a bubble in a laminar duct flow, Adv. Multiphase Flow (Elsevier) (1995) 3–15.

[43] M.J. Raw, A coupled algebraic multigrid method for the 3D Navier–Stokes equations, in: Proceedings of the 10th GAMM Seminar, 1994.
[44] T.J. Barth, D.C. Jesperson, The design and application of upwind schemes on unstructured meshes, AIAA Paper 89-0366, 1989.
[45] C.M. Rhie, W.L. Chow, A numerical study of the turbulent flow past an isolated airfoil with trailing edge separation, AIAA Paper 82-0998, 1982.
[46] M.J. Raw, Robustness of coupled algebraic multigrid for the Navier–Stokes equations, in: Proceedings of the 34th Aerospace and Sciences Meeting & Exhibit, AIAA 96-0297, 1996.
[47] K.C. Ruthiya, V.P. Chilekar, M.J.F. Warnier, J. van der Schaaf, B.F.M. Kuster, J.C. Schouten, J.R. van Ommen, Detecting regime transitions in slurry bubble columns using pressure time series, AIChE J. 51 (2005) 1951–1965.
[48] C. Vial, E. Camarasa, S. Poncin, G. Wild, N. Midoux, J. Bouillard, Study of hydrodynamic behavior in bubble columns and external loop airlift reactors through analysis of pressure fluctuations, Chem. Eng. Sci. 55 (2000) 2957–2973.
[49] M.E. Diaz, F.J. Montes, M.A. Galan, Influence of aspect ratio and superficial gas velocity on the evolution of unsteady flow structures and flow transitions in a rectangular two-dimensional bubble column, Ind. Eng. Chem. Res. 45 (2006) 7301–7312.
[50] T. Frank, Development of CFD Software for the Simulation of Multidimensional Flows in the Reactor Cooling Systems, AEA Technology/ANSYS-CFX, 2003.
[51] E. Krepper, B.N. Reddy Vanga, A. Zaruba, H.-M. Prasser, M.A. Lopez de Bertodano, Experimental and numerical studies of void fraction distribution in rectangular bubble columns, Nucl. Eng. Design 237 (2007) 399–408.
[52] M. Milelli, A numerical Analysis of Confined Turbulent Bubble Plume, ETH No. 14799, Swiss Federal Institute of Technology, Zurich, 2002.
[53] D. Lakehal, B.L. Smith, M. Milelli, Large-eddy simulation of bubbly turbulent shear flows, J. Turb. 3 (2002) 0–25.
[54] M.C. Ruzicka, J. Zahradnik, J. Drahoš, N.H. Thomas, Homogeneous–heterogeneous regime transition in bubble columns, Chem. Eng. Sci. 56 (2001) 4609–4626.
[55] J. Zahradnik, M. Fialovfi, M. Ruzicka, J. Drahoš, F. Kastanek, N.H. Thomas, Duality of the gas–liquid flow regimes in bubble column reactors, Chem. Eng. Sci. 52 (1997) 3811–3826.
[56] P. Chen, J. Sanyal, M.P. Dudukovic, Numerical simulation of bubble columns flows: effect of different breakup and coalescence closures, Chem. Eng. Sci. 60 (2005) 1085–1101.
[57] D. Darmana, R.L.B. Henket, N.G. Deen, J.A.M. Kuipers, Detailed modelling of hydrodynamics, mass transfer and chemical reactions in a bubble column using a discrete bubble model: chemisorption of CO_2 into NaOH solution, numerical and experimental study, Chem. Eng. Sci. 62 (2007) 2556–2575.
[58] E. Camarasa, C. Vial, S. Poncin, G. Wild, N. Midoux, J. Bouillard, Influence of coalescence behavior of the liquid and of gas sparging on hydrodynamics and bubble characteristics in a bubble column, Chem. Eng. Process. 38 (1999) 329–344.